Broadband infrared vibrational nano-spectroscopy using thermal blackbody radiation

Brian T. O'Callahan, William E. Lewis, Silke Möbius, Jared C. Stanley, Eric A. Muller, and Markus B. Raschke*

Department of Physics, Department of Chemistry, and JILA, University of Colorado at Boulder, Boulder, CO 80309, USA

*markus.raschke@colorado.edu

Abstract: Infrared vibrational nano-spectroscopy based on scattering scanning near-field optical microscopy (*s*-SNOM) provides intrinsic chemical specificity with nanometer spatial resolution. Here we use incoherent infrared radiation from a 1400 K thermal blackbody emitter for broadband infrared (IR) nano-spectroscopy. With optimized interferometric heterodyne signal amplification we achieve few-monolayer sensitivity in phonon polariton spectroscopy and attomolar molecular vibrational spectroscopy. Near-field localization and nanoscale spatial resolution is demonstrated in imaging flakes of hexagonal boron nitride (hBN) and determination of its phonon polariton dispersion relation. The signal-to-noise ratio calculations and analysis for different samples and illumination sources provide a reference for irradiance requirements and the attainable near-field signal levels in *s*-SNOM in general. The use of a thermal emitter as an IR source thus opens *s*-SNOM for routine chemical FTIR nano-spectroscopy.

OCIS codes: (180.4243) Near-field microscopy; (300.6340) Spectroscopy, infrared.

References and links

1. B. Knoll and F. Keilmann, "Near-field probing of vibrational absorption for chemical microscopy," Nature **399**, 134–137 (1999).
2. J. M. Atkin, S. Berweger, A. C. Jones, and M. B. Raschke, "Nano-optical imaging and spectroscopy of order, phases, and domains in complex solids," Adv. Phys. **61**, 745–842 (2012).
3. F. Keilmann and R. Hillenbrand, "Near-field microscopy by elastic light scattering from a tip," Philos. T. Roy. Soc. A **362**, 787–805 (2004).
4. S. Amarie, P. Zaslansky, Y. Kajihara, E. Griesshaber, W. W. Schmahl, and F. Keilmann, "Nano-FTIR chemical mapping of minerals in biological materials," Beilstein Journal of Nanotechnology **3**, 312–323 (2012).
5. F. Huth, A. Govyadinov, S. Amarie, W. Nuansing, F. Keilmann, and R. Hillenbrand, "Nano-FTIR absorption spectroscopy of molecular fingerprints at 20 nm spatial resolution," Nano Lett. **12**, 3973–3978 (2012). PMID: 22703339.
6. X. G. Xu and M. B. Raschke, "Near-field infrared vibrational dynamics and tip-enhanced decoherence," Nano Lett. **13**, 1588–1595 (2013). PMID: 23387347.
7. I. Amenabar, S. Poly, W. Nuansing, E. H. Hubrich, A. A. Govyadinov, F. Huth, R. Krutokhvostov, L. Zhang, M. Knez, J. Heberle, A. M. Bittner, and R. Hillenbrand, "Structural analysis and mapping of individual protein complexes by infrared nanospectroscopy," Nat. Commun. **4**, 2890 (2013).
8. S. Berweger, D. M. Nguyen, E. A. Muller, H. A. Bechtel, T. T. Perkins, and M. B. Raschke, "Nano-chemical infrared imaging of membrane proteins in lipid bilayers," J. Am. Chem. Soc. **135**, 18292–18295 (2013).
9. C. Westermeier, A. Cernescu, S. Amarie, C. Liewald, F. Keilmann, and B. Nickel, "Sub-micron phase coexistence in small-molecule organic thin films revealed by infrared nano-imaging," Nat. Commun. **5**, 4101 (2014).

#250910 Received 2 Oct 2015; revised 6 Nov 2015; accepted 10 Nov 2015; published 3 Dec 2015

10. B. Pollard, E. A. Muller, K. Hinrichs, and M. B. Raschke, "Vibrational nano-spectroscopic imaging correlating structure with intermolecular coupling and dynamics," Nat. Commun. **5** (2014).
11. F. Peragut, J.-B. Brubach, P. Roy, and Y. De Wilde, "Infrared near-field imaging and spectroscopy based on thermal or synchrotron radiation," Appl. Phys. Lett. **104**, 251118 (2014).
12. E. A. Muller, B. Pollard, and M. B. Raschke, "Infrared chemical nano-imaging: Accessing structure, coupling, and dynamics on molecular length scales," J. Phys. Chem. Lett. **6**, 1275–1284 (2015).
13. H. A. Bechtel, E. A. Muller, R. L. Olmon, M. C. Martin, and M. B. Raschke, "Ultrabroadband infrared nanospectroscopic imaging," Proc. Nat. Acad. Sci. USA **111**, 7191–7196 (2014).
14. P. Hermann, A. Hoehl, G. Ulrich, C. Fleischmann, A. Hermelink, B. Kästner, P. Patoka, A. Hornemann, B. Beckhoff, E. Rühl, and G. Ulm, "Characterization of semiconductor materials using synchrotron radiation-based near-field infrared microscopy and nano-FTIR spectroscopy," Opt. Express **22**, 17948–17958 (2014).
15. Y. D. Wilde, F. Formanek, R. Carminati, B. Gralek, P. Lemoine, K. Joulain, J. Mulet, Y. Chen, and J. Greffet, "Thermal radiation scanning tunneling microscopy," Nature **444**, 740–743 (2006).
16. A. Jones and M. B. Raschke, "Thermal infrared near-field spectroscopy." Nano Letters **12**, 1475–1481 (2012).
17. Y. Kajihara, K. Kosaka, and S. Komiyama, "Thermally excited near-field radiation and far-field interference," Opt. Express **19**, 7695–7704 (2011).
18. F. Huth, M. Schnell, J. Wittborn, N. Ocelic, and R. Hillenbrand, "Infrared-spectroscopic nanoimaging with a thermal source," Nat. Mater. **10**, 352–356 (2011).
19. M. Ishikawa, M. Katsura, S. Nakashima, Y. Ikemoto, and H. Okamura, "Broadband near-field mid-infrared spectroscopy and application to phonon resonances in quartz," Opt. Express **20**, 11064–11072 (2012).
20. A. A. Govyadinov, S. Mastel, F. Golmar, A. Chuvilin, P. S. Carney, and R. Hillenbrand, "Recovery of permittivity and depth from near-field data as a step toward infrared nanotomography," ACS Nano **8**, 6911–6921 (2014).
21. S. Dai, Z. Fei, Q. Ma, A. S. Rodin, M. Wagner, A. S. McLeod, M. K. Liu, W. Gannett, W. Regan, K. Watanabe, T. Taniguchi, M. Thiemens, G. Dominguez, A. H. C. Neto, A. Zettl, F. Keilmann, P. Jarillo-Herrero, M. M. Fogler, and D. N. Basov, "Tunable phonon polaritons in atomically thin van der waals crystals of boron nitride," Science **343**, 1125–1129 (2014).
22. Z. Shi, H. A. Bechtel, S. Berweger, Y. Sun, B. Zeng, C. Jin, H. Chang, M. C. Martin, M. B. Raschke, and F. Wang, "Amplitude- and phase-resolved nanospectral imaging of phonon polaritons in hexagonal boron nitride," ACS Photonics **2**, 790–796 (2015).
23. R. Geick, C. H. Perry, and G. Rupprecht, "Normal modes in hexagonal boron nitride," Phys. Rev. **146**, 543–547 (1966).
24. J. D. Caldwell, A. V. Kretinin, Y. Chen, V. Giannini, M. M. Fogler, Y. Francescato, C. T. Ellis, J. G. Tischler, C. R. Woods, A. J. Giles, M. Hong, K. Watanabe, T. Taniguchi, S. A. Maier, and K. S. Novoselov, "Sub-diffractional volume-confined polaritons in the natural hyperbolic material hexagonal boron nitride," Nat. Commun. **5**, 6221 (2014).
25. S. Bensmann, F. Gaußmann, M. Lewin, J. Wüppen, S. Nyga, C. Janzen, B. Jungbluth, and T. Taubner, "Near-field imaging and spectroscopy of locally strained GaN using an IR broadband laser," Opt. Express **22**, 22369–22381 (2014).
26. B. Knoll and F. Keilmann, "Enhanced dielectric contrast in scattering-type scanning near-field optical microscopy," Opt. Commun. **182**, 321–328 (2000).
27. M. K. Gunde, "Vibrational modes in amorphous silicon dioxide," Physica B: Condensed Matter **292**, 286–295 (2000).
28. C. Y. Liang and S. Krimm, "Infrared spectra of high polymers. iii. polytetrafluoroethylene and polychlorotrifluoroethylene," The Journal of Chemical Physics **25**, 563–571 (1956).
29. E. H. Korte and A. Röseler, "Infrared reststrahlen revisited: commonly disregarded optical details related to n<1," Analytical and Bioanalytical Chemistry **382**, 1987–1992 (2005).
30. S. Mastel, A. A. Govyadinov, T. V. A. G. de Oliveira, I. Amenabar, and R. Hillenbrand, "Nanoscale-resolved chemical identification of thin organic films using infrared near-field spectroscopy and standard fourier transform infrared references," Appl. Phys. Lett. **106**, 023113 (2015).
31. G. Masetti, F. Cabassi, G. Morelli, and G. Zerbi, "Conformational order and disorder in poly(tetrafluoroethylene) from the infrared spectrum," Macromolecules **6**, 700–707 (1973).
32. S. Amarie and F. Keilmann, "Broadband-infrared assessment of phonon resonance in scattering-type near-field microscopy," Phys. Rev. B **83**, 045404 (2011).
33. S. Dai, Q. Ma, T. Andersen, A. S. Mcleod, Z. Fei, M. K. Liu, M. Wagner, K. Watanabe, T. Taniguchi, M. Thiemens, F. Keilmann, P. Jarillo-Herrero, M. M. Fogler, and D. N. Basov, "Subdiffractional focusing and guiding of polaritonic rays in a natural hyperbolic material," Nat. Commun. **6**, 6963 (2015).
34. J. M. Atkin, P. M. Sass, P. E. Teichen, J. D. Eaves, and M. B. Raschke, "Nanoscale probing of dynamics in local molecular environments," J. Phys. Chem. Lett. **6**, 4616–4621 (2015).
35. R. L. Olmon and M. B. Raschke, "Antenna-load interactions at optical frequencies: impedance matching to quantum systems," Nanotechnology **23**, 444001 (2012).
36. L. Mandel and E. Wolf, *Optical Coherence and Quantum Optics* (Cambridge University, 1995) (Chap. 13).

#250910 Received 2 Oct 2015; revised 6 Nov 2015; accepted 10 Nov 2015; published 3 Dec 2015

1. Introduction

Near-field infrared vibrational nano-imaging and -spectroscopy in the implementation of infrared scattering scanning near-field optical microscopy (IR *s*-SNOM) has emerged as a powerful technique for chemical nano-imaging [1]. Analogous to conventional far-field FTIR spectroscopy and microscopy it provides chemical specificity, yet with diffraction-unlimited nanometer spatial resolution [2, 3]. IR *s*-SNOM has recently demonstrated its potential for the study of even complex and multicomponent soft-matter and biomaterials down to molecular length scales [4–10].

However, stringent infrared light source requirements have so far prevented IR *s*-SNOM from becoming a routine technique. Both continuous wave and femtosecond laser based IR sources have found their respective application space for *s*-SNOM [11, 12]. Yet for true chemical nano-FTIR spectroscopy, broadband IR radiation that spans the full mid-IR spectral range is desired from the few 100's of cm^{-1} finger print region up to $\sim$ 4000 cm^{-1} for the highest frequency normal modes (spanning 3 octaves). Such broadband IR *s*-SNOM spectroscopy has been enabled using synchrotron IR radiation with its high spectral irradiance [13, 14] or based on the enhanced local optical density of states of thermal near-field radiation [11, 15–17].

A simple blackbody thermal source in the form of tungsten or ceramic filaments can provide comparable IR bandwidth. Its use has been demonstrated for *s*-SNOM [18, 19], however, over a limited spectral range, with low signal-to-noise ratio, and only for the strong responses of collective phonon polaritons of SiO_2 or free carriers of doped Si. Despite the compelling simplicity, low cost, and low irradiance noise, the use of a thermal emitter as a light source for *s*-SNOM has so far not been explored further.

In this work we demonstrate IR *s*-SNOM nano-spectroscopy using a blackbody emitter with high sensitivity based on improved source and tip illumination and an optimized short-path asymmetric Michelson interferometer. Using optical interferometric heterodyne near-field amplification and detection, the complex-valued nanoscale vibrational material response is obtained. In addition to the nano-spectroscopy and -imaging of the surface phonon polariton of SiO_2, we resolve the phonon polariton response and its dispersion of hexagonal boron nitride (hBN), with thicknesses as low as 8 nm (25 monolayers), and demonstrate the extension to the two orders-of-magnitude weaker molecular resonances of C-F vibrational modes in polytetrafluoroethylene (PTFE) as an example. Despite the incoherent nature of the radiation and the associated low spectral irradiance, this work shows the general feasibility of the use of a thermal emitter as a light source for nano-spectroscopy for a broader range of *s*-SNOM applications than previously considered.

2. Experiment

The *s*-SNOM setup as shown in Fig. 1(a) is based on a modified atomic force microscope (AFM) (Vesta AFM-SP, Anasys Instruments) operated in dynamic mode, with asymmetric heterodyne interferometric signal detection [2], and dry air purge enclosure to reduce atmospheric absorption by more than a factor of 2 and allows us to investigate vibrational modes in the water absorption region, e.g., the in-plane mode of hBN. A heated ceramic globar (EverGlo, Thermo-Fisher, IR emissivity $\varepsilon \approx 0.9$) operating at $T \simeq 1400$ K provides IR thermal blackbody radiation, which is collected with an off-axis parabolic mirror ($f = 50$ mm, $\phi = 25$ mm, NA = 0.24). Light passes through the KBr beamsplitter (BS) with a transmission coefficient of 50% and is focused onto the AFM tip by another high-NA off-axis parabolic mirror ($f = 20.8$ mm, NA $= 0.48$). Commercial dynamic mode metallic AFM tips (Arrow NCPt, NanoWorld) provide local field enhancement of the incident IR radiation and act as local near-field probes of the sample optical properties with spatial resolution determined by the tip apex radius (typically $10 - 20$ nm). The mirror position in the reference arm is controlled with a closed loop delay

#250910 Received 2 Oct 2015; revised 6 Nov 2015; accepted 10 Nov 2015; published 3 Dec 2015

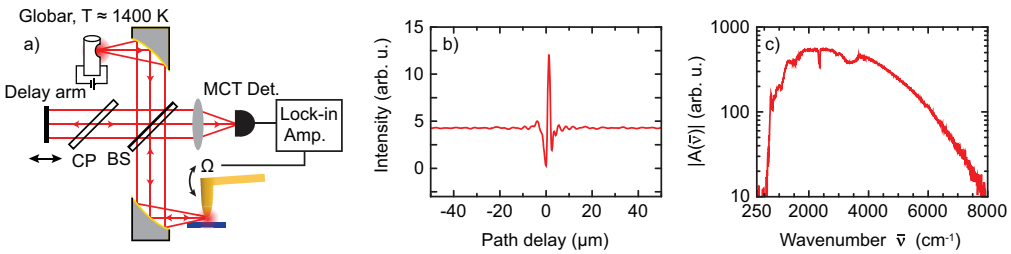

Fig. 1. (a) Schematic of infrared nano-spectroscopy using broadband infrared thermal radiation from a ceramic globar, utilizing heterodyne detection by asymmetric Michelson interferometry with beamsplitter (BS), compensation plate (CP) and mercury-cadmium-telluride (MCT) detector. (b) Reference interferogram of blackbody source. (c) Corresponding broadband Fourier transform of (b).

stage with 50 mm maximum travel distance corresponding to a spectral resolution limit of 0.1 cm^{-1} (ANT95-50-L, Aerotech). The compensation plate (CP) in the reference arm accounting for the beamsplitter substrate thickness facilitates the extraction of near-field phase spectra which aids in the identification of vibrational modes. Short beam paths in both signal and reference arm of length ≈ 9 cm provide high stability (sub-250 nm mean drift in 30 min) and ease of alignment. The short beam path further helps to increase the infrared fluence at the tip due to the limited beam collimation of the blackbody source. After interference with the reference beam, the tip-scattered light is focused by an off-axis parabolic mirror ($f = 10$ cm, $\phi = 25$ mm, NA = 0.12) onto a mercury-cadmium-telluride (MCT) detector (J15D14-M204-S250U-30, EG&G, peak specific detectivity $D^* = 4 \cdot 10^{10}$ $\sqrt{\text{Hz}}/\text{cm}^{-1}$ W^{-1}).

Lock-in demodulation on the first and second harmonics of the cantilever tapping frequency Ω provides for effective far-field background suppression at tapping amplitudes below ~ 80 nm. Approach curves (see appendix) verify the near-field content of the first harmonic, with an order of magnitude signal increase when in contact with the surface with a $1/e$ decay length of ~ 60 nm. All data in this paper are reported for first harmonic demodulation, which is found to be sufficient for far-field background suppression while providing high quality spectra. Typically, demodulation at higher orders of the cantilever tapping frequency ($n\Omega$ for $n \geq 2$) is desirable for high near-field contrast and improved spatial resolution [20], however for smooth samples with low scattering the first harmonic can suffice for near-field detection with tapping amplitudes $\lesssim 80$ nm. With proper alignment and high quality beam focus we also observe sufficient background suppression at first harmonic in approach curves and imaging on even highly scattering samples. We acquire interferograms by collecting the real component of the lock-in signal while sweeping the delay by moving the reference arm. The delay stage is operated in a step-scan modality, with a step size of 500 nm and step dwell time ranging from $50 - 200$ ms, depending on signal strength. Typically 5-60 consecutive interferograms are averaged to improve signal-to-noise ratio. To reduce acquisition times and improve signal-to-noise at positive delays, we acquire interferograms asymmetrically around zero path delay. Corresponding asymmetric apodization is applied using the product of a Gaussian and an error function centered around zero path delay before performing the Fourier transform to extract the complex valued near-field spectrum. We normalize the amplitude spectrum by dividing by the gold reference amplitude spectrum. The gold phase spectrum is also subtracted from the sample phase spectrum.

Figure 1(b) shows an interferogram of the source radiation with corresponding Fourier transform spectrum (c). Broadband optics (KBr beamsplitter transmission window 400-30000

#250910 Received 2 Oct 2015; revised 6 Nov 2015; accepted 10 Nov 2015; published 3 Dec 2015

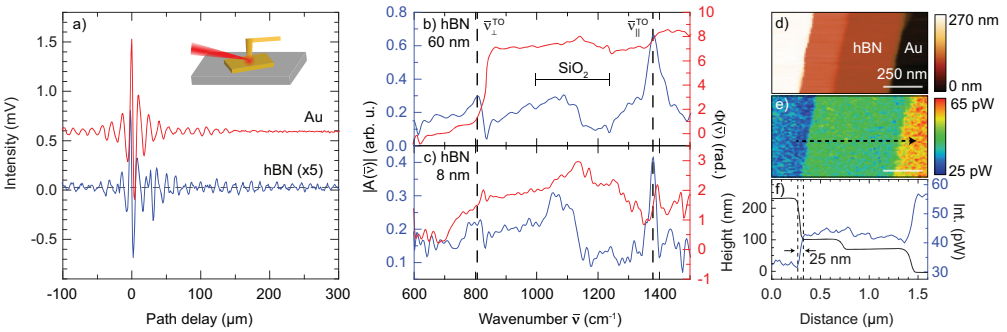

Fig. 2. Thermal source asymmetric *s*-SNOM interferograms of hexagonal boron nitride flake on SiO_2 (hBN, blue) and Au reference sample (red, offset for clarity) obtained at first harmonic demodulation (a). Normalized near-field amplitude and phase spectra acquired on a 60 nm ((b), integration time $t = 15$ minutes and spectral resolution $\delta\bar{\nu} = 26$ cm^{-1}) and a 8 nm thick flake ((c), $t = 56$ minutes, $\delta\bar{\nu} = 31$ cm^{-1}). AFM topography (d), and spectrally integrated optical image (e) across an hBN/Au step edge. Line traces shown in panel (f) correspond to the dashed line in panel (e) and show ~ 25 nm spatial resolution (5-95% signal level).

cm^{-1}), high source temperatures, and dry air purging extend the available bandwidth of previous studies [18, 19] with our bandwidth primarily limited by the sensitivity range of the MCT detector used. A high temperature thermal source ($T \approx 1400$ K) increases irradiance and further improves usable bandwidth. Blackbody radiation is focused on the tip with a beam waist FWHM diameter of $\sim 70\ \mu$m and spectrally integrated power of ~ 2.8 mW, giving a peak spectral irradiance of $I \sim 25$ mW/cm^2 cm^{-1} using the FWHM bandwidth value of 4000 cm^{-1}. The beam profile was measured by scanning a knife edge across the focus of the parabolic mirror (see appendix).

3. Results

We collect IR near-field spectra of the vibrational response of SiO_2, hBN flakes of multiple thicknesses, and PTFE. Typical near-field interferograms are shown in Fig. 2(a) obtained on gold (red) and hBN (blue). Due to the non-resonant response of gold in the mid-IR, interferograms are symmetric about zero path delay. In contrast, hBN yields an asymmetric interferogram with distinct oscillations persisting for long optical path delays arising from the phonon polariton resonance. Figures 2(b) and 2(c) show the resulting broadband Fourier-transform near-field amplitude (blue) and phase (red) spectra normalized to the Au reference spectrum for two hBN flakes on a SiO_2 substrate with flake thicknesses 60 nm (b) and 8 nm (c), respectively. The distinct peaks in the amplitude spectrum correspond to the out-of-plane and in-plane transverse optical (TO) phonon modes at $\bar{\nu}_\perp^{\mathrm{TO}} \simeq 800$ cm^{-1} and $\bar{\nu}_\parallel^{\mathrm{TO}} \simeq 1370$ cm^{-1}, respectively [23]. The broad dispersive feature in the amplitude spectra between 1000 cm^{-1} to 1200 cm^{-1} is the phonon polariton response of the SiO_2 substrate. It is more pronounced relative to the in-plane TO phonon mode of hBN for the thinner flake, as expected. Despite the longer integration time for the 8 nm thick flake (56 min) than the 60 nm thick flake (15 min), the signal-to-noise ratio of the phonon modes is smaller for the thinner flake due to the decreased material volume in the near-field probe region. In addition, we see an increase of the linewidth of the in-plane phonon polariton response with increasing thickness. This linewidth increase is not due to defects as we verify by the thickness independent linewidth of the TO phonon mode measured by Raman spectroscopy of both samples (not shown). Instead, we attribute the increase in linewidth to in-

#250910 Received 2 Oct 2015; revised 6 Nov 2015; accepted 10 Nov 2015; published 3 Dec 2015

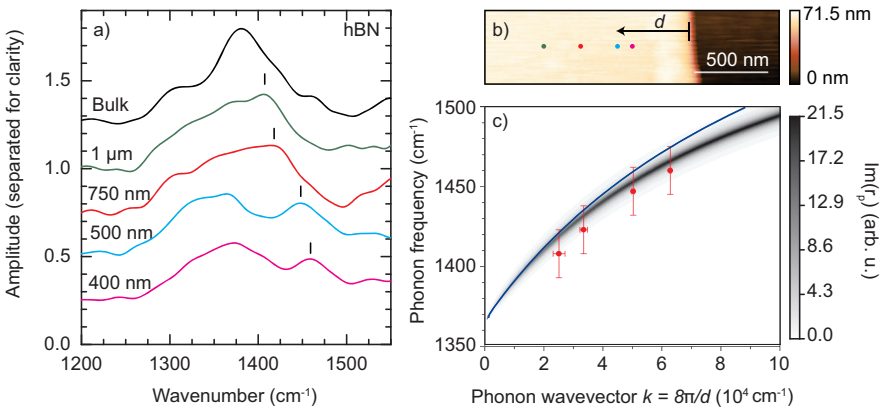

Fig. 3. (a) Spatially resolved spectra near an hBN edge with emergence of blue-shifted resonance near the in-plane TO phonon peak at 1370 cm^{-1} due to the constructive interference of phonon polaritons excited by the tip and reflected by the edge. (b) Topography of the $\sim$ 60 nm thick flake with the colored points representing the acquisition positions of the spectra in (a). Distance d from the edge is indicated. (c) Dispersion relation of the phonon polaritons with red points extracted from the spectra in (a). Grayscale plot is Im(r_p) calculated using results from [21]. Blue line is the dispersion relation based on the model presented in [22].

creasingly bulk-like polariton properties for thicker flakes, and the formation of the associated Reststrahlen band [24].

Figure 2(d) and 2(e) show AFM topography and near-field signal acquired simultaneously across an hBN/Au step edge. Spectrally integrated images were obtained with the reference arm at zero path difference for maximum heterodyne amplification. Line traces (dashed line in Fig. 2(e)) show $\simeq$ 25 nm spatial resolution limited only by the apex radius of the tip. Strong near-field contrast is observed with a large signal on Au due to its high Drude response. The spatial image also shows a strong contrast across the $\sim$ 140 nm step between the 100 nm and 240 nm thick sections of hBN (left) and the absence of discernible contrast for the $\sim$ 25 nm step between the 75 nm and the 100 nm regions (center).

The correlation of contrast with step height results from the finite IR *s*-SNOM probe depth within hBN and thus a variable residual IR contribution from the Au substrate depending on flake thickness. The amount of the contrast is then determined by the relative change in height across the hBN flake, i.e. larger for the greater step height compared to the smaller one. As the *s*-SNOM probe depth decreases for increasing harmonic orders, the observed contrast between the 100 nm and 240 nm thick hBN layers is larger than would otherwise be expected for second or higher order harmonic demodulation [20].

The heterodyne amplified signal can contain different spectral information depending on the fixed delay length of the reference arm [25]. By imaging at zero path difference, the nonresonant Drude response from gold dominates compared to the resonant phonon response of the hBN. In the case of a longer reference arm delay the contrast can be dominated by the long-lived phonon modes of hBN and contrast may be reversed.

In addition, due to the low absorption of hBN at infrared frequencies outside of the Reststrahlen bands and the associated finite IR penetration depth through the flake, incident IR light may propagate through the hBN flake and reflect off the Au substrate. This reflection would vary depending on flake thickness and may cause variations in the homodyne background that

#250910 Received 2 Oct 2015; revised 6 Nov 2015; accepted 10 Nov 2015; published 3 Dec 2015

may amplify the near field contrast between the 100 nm and the 240 nm thick flakes.

Figure 3(a) shows spatially resolved *s*-SNOM spectra acquired at different distances from the edge of a ~ 60 nm thick hBN flake. At $< 1\ \mu$m proximity to the edge (positions indicated in Fig. 3(b)), a second peak appears at frequencies higher than the in-plane TO phonon peak of 1370 cm^{-1}. This second peak, which continuously blue-shifts with decreasing tip-edge distance, is due to tip-excited phonon polaritons that reflect at the edge and constructively interfere with the incoming field at the tip position, as established previously [21, 22]. Spatial resolution of better than 100 nm is demonstrated through the resolution of the ~ 10 cm^{-1} blue shift of this peak from 500 to 400 nm positions. Figure 3(c) shows the resulting dispersion of the phonon polaritons (red points) extracted from the peak positions in Fig. 3(a). The wavevectors are given by the cavity condition of constructive interference $d = \lambda/4 = 8\pi/k$, where d is the distance from the hBN flake edge. Error in the wavevectors is determined by the uncertainty in d during the scan due to sample drift, and the error in the phonon frequencies is determined by the spectral resolution. The results are in good agreement with the phase space dispersion relation calculated from the imaginary part of the reflection coefficient r_p of the air/hBN/SiO_2 system [21] (grayscale plot), and the dispersion relation of 2D polaritons in the long wavelength limit [22] (blue line).

Figure 4(a) shows near-field spectra of a 300 nm thick amorphous SiO_2 layer on a Si substrate. The amplitude (blue) and phase (red) spectra are in good agreement with predictions from the point dipole model describing the tip-sample interaction [26]. The dielectric function for SiO_2 is calculated using a Lorentzian oscillator model with three phonon modes at frequencies $\bar{\nu} = 447$ cm^{-1}, 811 cm^{-1}, and 1050 cm^{-1}, with FWHM linewidths $\gamma = 49$ cm^{-1}, 69 cm^{-1}, and 70 cm^{-1}, and relative oscillator strengths $0.923, 0.082,$ and 0.663, respectively [27].

Figure 4(b) shows near-field amplitude and phase spectra of a $\sim 5\ \mu$m thick section of PTFE. Two distinct vibrational resonances around 1150 cm^{-1} and 1220 cm^{-1} are resolved in the phase spectrum, corresponding to the symmetric $\bar{\nu}_s$ and antisymmetric $\bar{\nu}_{as}$ C-F stretch modes, respectively (dashed vertical lines). Given the lateral spatial resolution of 100 nm demonstrated in Fig. 3 with corresponding probe volume of $\sim (100\ \text{nm})^3$ and a molar volume of $0.02\ \text{mol}/\text{cm}^3$, this corresponds to 20 attomol sensitivity of the C-F vibrational mode of PTFE. The near-field amplitude and phase spectra (solid lines) approximate the real and imaginary parts of the index of refraction [6], with their corresponding dispersive and absorptive features, respectively [28,29].

Although the appearance of symmetric and antisymmetric modes were reproducible between consecutive scans, we observed spectral variations at different positions across the PTFE sample. Sample drift across spectrally distinct nanoscale regions during measurements limits integration time to $t \leq 5$ min and prevents summation of many acquisitions. Though there can be spectral shifts due to sample thickness observed in *s*-SNOM, in the limit of film thickness much larger than tip radius these effects become negligible [30]. This spatial heterogeneity in the spectral features may be due to local variations in the polymer chain order and crystallinity [31].

4. Discussion

In the following, we analyze the normalized signal-to-noise ratios (NSNR) normalized by spectral resolution and acquisition time for the different samples (Fig. 5). The NSNR is defined by $\text{NSNR} = \frac{\text{signal power}}{\text{rms noise}} / (\delta\bar{\nu}\sqrt{t})$ where $\delta\bar{\nu}$ is the spectral resolution and t is the integration time of the spectrum. The calculated NSNRs allow us to compare published results using different *s*-SNOM sources with spectra collected at different resolutions and acquisition times.

NSNRs determined from amplitude data in Figs. 2b),c) and 3a),b) range from 0.001 $\sqrt{\text{Hz}}/\text{cm}^{-1}$ up to 0.02 $\sqrt{\text{Hz}}/\text{cm}^{-1}$. We compare these thermal source near-field NSNRs to the range of signal levels and their NSNRs from *s*-SNOM data based on other light sources

#250910 Received 2 Oct 2015; revised 6 Nov 2015; accepted 10 Nov 2015; published 3 Dec 2015

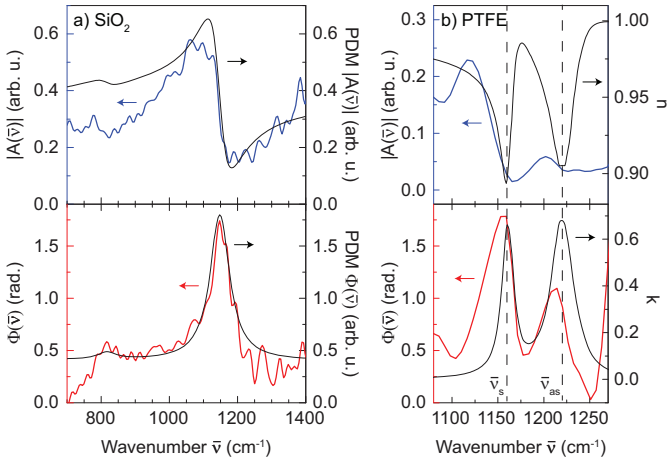

Fig. 4. Near-field magnitude (blue) and phase (red) spectra for (a) a 300 nm thick amorphous SiO_2 layer and (b) PTFE. Spectra were obtained with integration times of 30 min and 5 min, and spectral resolution of 26 cm^{-1} and 21 cm^{-1} for SiO_2 and PTFE, respectively. The SiO_2 spectrum matches the predictions from the point dipole model (PDM) over a broad spectral range. The PTFE near-field spectrum is plotted in comparison with the complex index of refraction $n(\bar{\nu})$ and $k(\bar{\nu})$ [29].

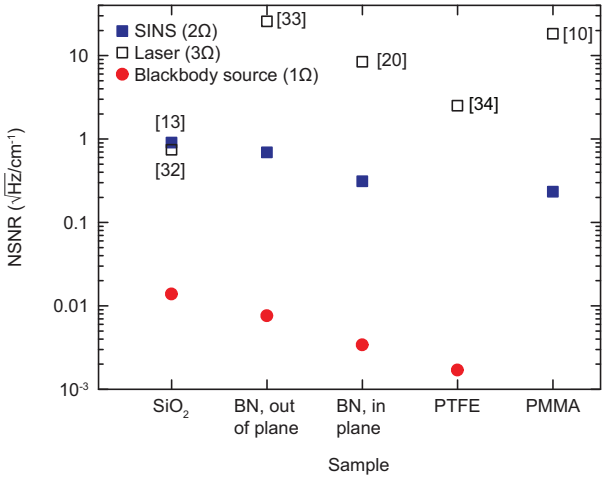

Fig. 5. Signal-to-noise ratio analysis for *s*-SNOM spectra of different samples using the thermal blackbody source (red, first harmonic), synchrotron infrared near-field spectroscopy (SINS) (blue, second harmonic) and different laser sources (black, third harmonic). NSNR analysis for published work are referenced [X] with corresponding citation number.

#250910 Received 2 Oct 2015; revised 6 Nov 2015; accepted 10 Nov 2015; published 3 Dec 2015

as displayed in Fig. 5. The extracted NSNRs from synchrotron infrared nano-spectroscopy (SINS) [13] with demodulation at the second harmonic of the tip dither frequency (2Ω) is consistently almost two orders-of-magnitude higher than that from our blackbody source demodulated at the first harmonic of the tip (Ω). Furthermore, several NSNRs for laser based near-field spectroscopy obtained at 3Ω [10, 21, 32–34] are included for reference. In general, higher NSNRs are possible with laser sources but they vary widely, often limited by laser stability, noise, and irradiance fluctuations across the mid-infrared. While the NSNRs are normalized by spectral resolution and acquisition time, we do not account for the typically weaker signal strengths with increasing harmonic order [26]. Note that our NSNRs are extracted from the amplitude spectra normalized by dividing by a reference spectrum, which may add additional noise that would not be present in unnormalized spectra.

The estimated irradiance incident on the tip using the blackbody source is $I \sim 25$ mW/(cm^2 cm^{-1}). This is in general 1-2 orders of magnitude less than that available with SINS, which ranges from $0.1-1$ W/(cm^2 cm^{-1}). The large difference in irradiance is in part due to the large focal spot of the spatially incoherent thermal radiation compared to coherent synchrotron radiation. Although the tip scattered near-field can be treated as Rayleigh point-dipole emission from the apex vicinity exhibiting approximately planar wavefronts, the large incident beam spot reduces the driving field strength at the tip. We estimate the peak field strength at the tip to be 280 V/cm, and the spectrally integrated intensity across the cross-sectional area of the 25 nm radius tip apex to be 0.5 nW.

Tunable continuous wave laser sources can achieve the highest spectral irradiance with NSNRs greater than 10 $\sqrt{\text{Hz}}$/cm^{-1}, e.g., for PMMA [10], or hBN [21, 33], albeit at the expense of wavelength tuning range. Note that the carbonyl vibrational resonance, though relatively strong, is weaker than the C-F vibrational mode of PTFE, and could not be observed in our *s*-SNOM measurements using the blackbody source. Ultrafast laser sources allow for broader spectral bandwidth, with typical irradiances of over 10 W/(cm^2 cm^{-1}). In particular, the 3 orders of magnitude higher spectral irradiance compared to the blackbody source yields correspondingly higher NSNRs (e.g., PTFE, with a NSNR of ~ 2.5 $\sqrt{\text{Hz}}$/cm^{-1} attained at 3Ω) [34].

In the following, we estimate the signal strength and degree of heterodyne amplification. The intensity at the detector includes contributions from the tip scattered near-field E_{nf}, the uncontrolled background scattered from the tip-shaft and the sample E_{bkg}, and the reference field E_{ref}, given by:

$$I = |E_{\text{nf}} + E_{\text{bkg}} + E_{\text{ref}}|^2 \tag{1}$$

$$\begin{aligned} &= |E_{\text{nf}}|^2 + |E_{\text{bkg}}|^2 + |E_{\text{ref}}|^2 + 2\cdot\text{Re}\left(E_{\text{bkg}}^* E_{\text{ref}}\right) \\ &+ 2\cdot\text{Re}\left(E_{\text{nf}}^* E_{\text{bkg}}\right) + 2\cdot\text{Re}\left(E_{\text{nf}}^* E_{\text{ref}}\right). \end{aligned} \tag{2}$$

The second, third, and fourth terms in the expanded equation are not modulated at the tip frequency and are thus suppressed by the lock-in detection. The first term is negligible compared to the remaining terms which are interferometrically amplified (described below). The last two terms describe the self-homodyne amplification by E_{bkg} which is delay-independent yielding a small offset in the interferograms (dashed line in Fig. 2(a)), and the delay-dependent heterodyne amplification of the near-field scattered light by E_{ref}, respectively.

We now use the characteristics of a typical interferogram (see Fig. 2(a)) to estimate the relative contributions from the remaining relevant terms in Eq. (2). At large negative delays, in the absence of interference with the reference arm, the small signal (dotted line) is from the term $2\cdot\text{Re}\left(E_{\text{nf}}^* E_{\text{bkg}}\right)$ only, which we estimate to be $20-100$ pW. Near zero path delay, the intensity is dominated by the $2\cdot\text{Re}\left(E_{\text{nf}}^* E_{\text{ref}}\right)$ term, with a peak power of $2-10$ nW. Based on the heterodyne amplification with a typical measured reference arm power of $P_{\text{ref}} \sim 3$ mW, this

#250910 Received 2 Oct 2015; revised 6 Nov 2015; accepted 10 Nov 2015; published 3 Dec 2015

corresponds to a tip scattered power of $P_{\mathrm{nf}} \sim 2-30$ fW. This value agrees well with estimates of the scattered power of a 25 nm radius metallic sphere near the sample surface from the point dipole model based on our incident fluence [26]. Similarly, we can estimate the background power to be $P_{\mathrm{bkg}} \sim 10\ \mu$W.

The lower bound of the unamplified tip-scattered power $P_{\mathrm{nf}} \sim 2$ fW corresponds to ~ 100 photons/s within 1 cm^{-1} bandwidth, which is approaching the shot noise limit for typical step-scan dwell times of ~ 100 ms. The self-homodyne and heterodyne amplification are thus crucial for the detection of such weak near-field signals. From the power estimates of P_{nf}, P_{bkg}, and P_{ref}, we estimate a self-homodyne intensity amplification factor of $\mathrm{Re}\left(E_{\mathrm{nf}}^{*}E_{\mathrm{bkg}}\right)/|E_{\mathrm{nf}}|^{2} \sim 10^{3}$ and a heterodyne intensity amplification factor of $\mathrm{Re}\left(E_{\mathrm{nf}}^{*}E_{\mathrm{ref}}\right)/|E_{\mathrm{nf}}|^{2} \sim 10^{5}$. These amplification steps result in more practical signal intensities well above the shot noise limit.

To further explore the limitation of low spectral irradiance on detectable *s*-SNOM signal levels, we acquired spectra at variable source temperature with a corresponding variation in intensity (Fig. 6). The NSNR versus irradiance is ideally described by $\mathrm{NSNR}(I) = A \cdot I/\left(\sqrt{I}+B\right)$ where A, B are fit parameters (dashed lines). This expression describes the roughly $\sqrt{I}$ dependence for large irradiance, with a small offset for the detector noise at zero irradiance. Near-field spectra of a 60 nm thick hBN flake could be obtained using an estimated peak spectral irradiance as low as $I \sim 2$ mW/cm^2/cm^{-1} at the tip apex and ≈ 40 pW spectrally integrated power incident on the cross-sectional area of the 25 nm radius tip, and a reference arm power $\approx 200\ \mu$W. The corresponding NSNR around the in-plane mode is found to be $\sim 1.2 \cdot 10^{-3}$ $\sqrt{\mathrm{Hz}}$/cm^{-1}, which for a typical acquisition time of 10^3 s and a spectral resolution of 20 cm^{-1} leads to a signal-to-noise ratio of only 0.75:1 for the in-plane mode and 2:1 for the out-of-plane mode. The NSNR increases rapidly with temperature for the in-plane mode due to the change in color temperature, and leads to a signal-to-noise ratio of, e.g., 2.3:1 for an irradiance of ~ 6 mW/cm^2/cm^{-1} measured under otherwise identical acquisition parameters as above. In comparison, the signal-to-noise ratio for the out-of-plane mode increases only by a factor of 2, to 4:1. Note that a unique feature of the use of a blackbody emitter as a source for *s*-SNOM in contrast to most laser sources is the observation that the NSNRs are in general higher for spectroscopy at low frequencies. This results from the combination of the antenna enhancement of the radiative *s*-SNOM signal [35] and the higher emission efficiency of a blackbody at lower energies.

Intensity noise from the thermal source is small (typical rms power fluctuations are $\approx 0.1\%$), and interferometer instability is minimized with the short beam path. The dominant noise source is detector noise, primarily in the form of $1/f$ noise from the photoconductive MCT detector, which can be reduced by demodulating at higher harmonics of the cantilever frequency. Detectors of smaller active area have correspondingly higher D* and can also increase NSNRs.

Due to the sub-wavelength size of the apex, the tip scatters near-field light akin to a point emitter, with spatially coherent wavefronts primarily polarized along the tip axis. However, the tip-scattered light is combined with incoherent and unpolarized light from the reference arm resulting in incomplete interference at the detector. A mode matched detector size can serve to mode filter the reference arm field by preferentially selecting the spatially coherent mode of smaller focus size, and thus can improve the fringe visibility of the interferograms. The poor beam quality arises from imperfect collimation of the spatially extended and incoherent blackbody source. The fraction of collimated, spatially coherent light is limited by the conservation of etendue of the optical system, primarily determined by the source collection optics as well as the source geometry and can be improved by collecting light from the source with high NA optics. The spatial coherence of the source phase fronts is fundamentally limited by the finite coherence length of the emitter within the focal volume of the collection optics. Due to the finite decay length l_{c} of the first-order field correlation functions of a blackbody on the

#250910 Received 2 Oct 2015; revised 6 Nov 2015; accepted 10 Nov 2015; published 3 Dec 2015

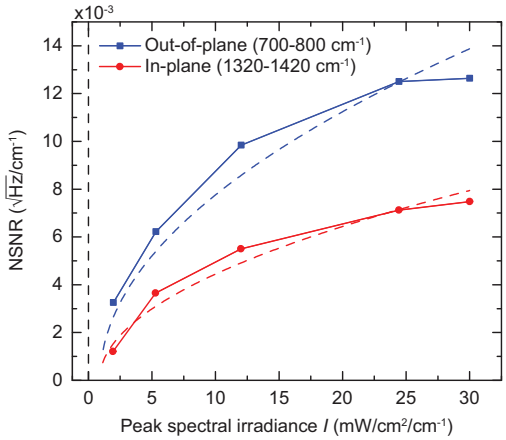

Fig. 6. NSNRs of the in-plane (red) and out-of-plane (blue) TO phonon response of hBN as a function of spectral irradiance I incident on the tip. The results were obtained by decreasing the temperature of the thermal source primarily resulting in a decrease in IR intensity. Dashed blue and red lines are fits to a theoretical $\mathrm{NSNR}(I) = A \cdot I / \left(\sqrt{I} + B\right)$ irradiance dependence.

order of $l_c \sim \hbar c / k_B T \sim 2\ \mu$m at $T = 1400$ K [36], collecting a spatially coherent mode from the blackbody source would require confocal and mode filtered collection and imaging of the source.

Despite these challenges, high quality spectra from just an 8 nm thick hBN flake demonstrates the high sensitivity of this technique. The spectrum from PTFE demonstrates the applicability of the technique to molecularly resonant materials and could allow its use for broadband chemical identification with nanoscale resolution.

5. Conclusion

We perform *s*-SNOM nanoscale spectroscopic measurements using a high bandwidth blackbody source, and a detector with spectral sensitivity from 700 cm^{-1} extending to the near-infrared. Optimized interferometric heterodyne detection and amplification extends the application space down to few monolayer phonon polariton spectroscopy and attomolar molecular vibrational spectroscopy. Signal strength and NSNRs are compared to nano-spectroscopy using synchrotron and laser-based IR sources across different samples. Calculated NSNRs versus source irradiance indicate that the technique is not limited by spectral irradiance of the blackbody source, and is still far from the limits of detector or source noise. We expect technical improvements on the setup, along with increasing capabilities of available thermal sources, to further enhance performance and expand application areas.

Appendix

Figure 7 shows the focal spot size of the thermal beam profile at the tip measured using a knife edge. Error function analysis shows that the focused beam profile is approximately Gaussian, with a FWHM of $\approx 70\ \mu$m. This is larger than the theoretical diffraction-limited spot size of $\sim 10\ \mu$m for a numerical aperture of $NA = 0.48$. We attribute this difference to the lack of spatial coherence across the phase front which is limited by the conservation of etendue of our optical system.

Figure 8 shows spectrally integrated and normalized approach curves of the optical signal

#250910 Received 2 Oct 2015; revised 6 Nov 2015; accepted 10 Nov 2015; published 3 Dec 2015

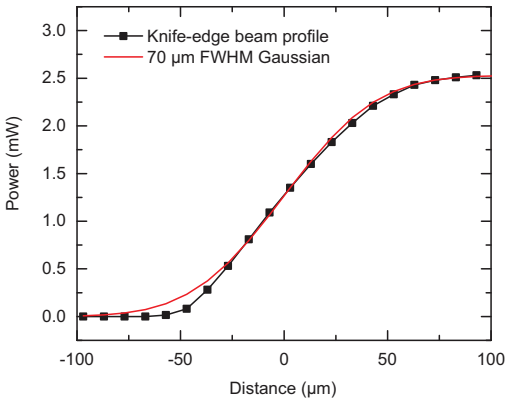

Fig. 7. Measurement of the focal spot at the tip using a knife edge technique. Data (black) is approximately described by a Gaussian intensity profile with FHWM of 70 μm (red).

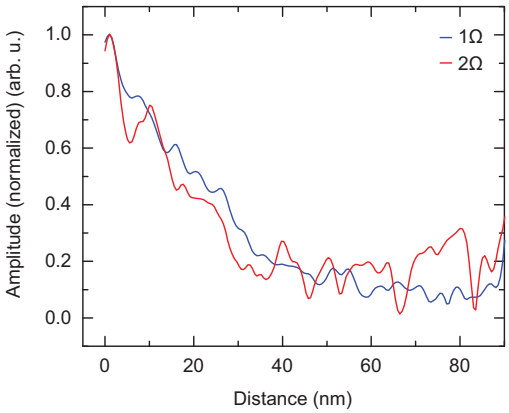

Fig. 8. Approach curves of the *s*-SNOM signal taken above a gold surface with reference arm at zero path difference. Demodulation at both the first (Ω) and second harmonic (2Ω) show strong near-field content with an order-of-magnitude increase within the last 50 nm.

at first (Ω) and second harmonic (2Ω) of the tip modulation frequency. Both contain strong near-field content with an order-of-magnitude increase within the last 50 nm. The approach curves were obtained with the reference arm at zero path difference for maximum heterodyne amplification.

Acknowledgments

We acknowledge Joanna Atkin for help developing the experiment. hBN samples were provided by Feng Wang and Samuel Berweger. Funding was provided by the U.S. Department of Energy, Office of Basic Sciences, Division of Material Sciences and Engineering, under Award No. DE-SC0008807. The ALS is supported by the Director, Office of Science, Office of Basic Energy Sciences, through the US Department of Energy (DOE) under Contract DE-AC02-05CH11231. We would like to acknowledge a partner proposal by the Environmental Molecular Sciences Laboratory (EMSL), a national scientific user facility from the DOE Office of Biological and Environmental Research at Pacific Northwest National Laboratory (PNNL). PNNL is operated by Battelle for the U.S. DOE under the contract DEAC06-76RL01830.